Soft x-ray absorption spectroscopy study of the electronic structures of the MnFe Prussian blue analogs $(Rb_xBa_y)Mn_{[3−(x+2y)]/2}[Fe(CN)_6]H_2O$

Eunsook Lee,[1] Seungho Seong,[1] Hyun Woo Kim,[1] D. H. Kim,[1,*] Nidhi Thakur,[2,†] S. M. Yusuf,[2] Bongjae Kim,[3] B. I. Min,[3]
Younghak Kim,[4] J.-Y. Kim,[4] F. M. F. de Groot,[5] and J.-S. Kang[1,‡]

[1]*Department of Physics, The Catholic University of Korea, Bucheon 14662, Korea*
[2]*Solid State Physics Division, Bhabha Atomic Research Centre, Mumbai 400 085, India*
[3]*Department of Physics, Pohang University of Science and Technology, Pohang 37673, Korea*
[4]*Pohang Accelerator Laboratory (PAL), Pohang University of Science and Technology, Pohang 37673, Korea*
[5]*Department of Inorganic Chemistry and Catalysis, Utrecht University, Sorbonnelaan 16, NL-3584 Utrecht, The Netherlands*

The electronic structures of Prussian blue analog $(Rb_xBa_y)Mn_{[3−(x+2y)]/2}[Fe(CN)_6]$ cyanides have been investigated by employing soft x-ray absorption spectroscopy (XAS) and magnetic circular dichroism (XMCD) at the Fe and Mn L ($2p$) edges. The measured XAS spectra have been analyzed with the configuration-interaction (CI) cluster model calculations. The valence states of the Fe and Mn ions are found to be Fe^{2+}-Fe^{3+} mixed valent, with an average valency of $v(Fe) \sim 2.8$ and nearly divalent (Mn^{2+}), respectively. Our Mn/Fe $2p$ XMCD study supports that Mn^{2+} ions are in the high-spin states while Fe^{2+}-Fe^{3+} ions are in the low-spin states. The Fe and Mn $2p$ XAS spectra are found to be essentially the same for $80 \leqslant T \leqslant 300$ K, suggesting that a simple charge transfer upon cooling from Fe^{3+}-CN-Mn^{2+} to Fe^{2+}-CN-Mn^{3+} does not occur in $(Rb_xBa_y)Mn_{[3−(x+2y)]/2}[Fe(CN)_6]$. According to the CI cluster model analysis, it is necessary to take into account both the ligand-to-metal charge transfer and the metal-to-ligand charge transfer in describing Fe $2p$ XAS, while the effect of charge transfer is negligible in describing Mn $2p$ XAS. The CI cluster model analysis also shows that the trivalent Fe^{3+} ions have a strong covalent bonding with the C ≡ N ligands and are under a large crystal-field energy of $10Dq \sim 3$ eV, in contrast to the weak covalency effect and a small $10Dq \sim 0.6$ eV for the divalent Mn^{2+} ions.

I. INTRODUCTION

Molecule-based magnetic materials exhibit several interesting switching phenomena between two electronic states in response to a magnetic field, light, pressure, and temperature, including a photoinduced magnetization transition [1–4], a pressure-induced magnetization transition [5], and a spin crossover [6]. Among them, Prussian blue analogs (PBAs), which are represented by the general formula $A_x M[M'(CN)_6]_y \cdot m H_2O$, where A is an alkali-metal cation and M and M' are divalent or trivalent transition-metal (TM) cations, have been studied extensively [6,7]. Both M and M' ions are located at the octahedral (O_h) sites [8,9]. Additional alkali-metal ions can be inserted in part of the interstitial tetrahedral (T_d) sites. CoFe and NiFe PBAs (M = Co,Ni; M' = Fe) crystallize in face-centered-cubic (fcc) structures, consisting of a three-dimensional (3D) coordination network containing Co-NC-Fe or Ni-NC-Fe entities [8]. Depending on A_x, MnFe PBAs (M = Mn; M' = Fe) exhibit diverse structural and magnetic phases. For example, some MnFe PBAs undergo structural phase transitions from an fcc ($F\bar{4}3m$) structure at high temperature (HT) to a tetragonal ($I\bar{4}m2$) structure at low temperature (LT) [6], with the concomitant switching phenomenon. The HT phase of $Rb_{0.88}Mn[Fe(CN)_6]_{0.96} \cdot m H_2O$ has a ferromagnetic stacking of antiferromagnetic sheets [10], while $(Rb_xBa_y)Mn_{[3−(x+2y)]/2}[Fe(CN)_6] \cdot m H_2O$ of the present study has an antiparallel stacking of ferromagnetic sheets along the crystallographic c direction (see Fig. 1) [11].

Understanding the physical and magnetic properties of the PBAs is very important, not only for their technical application but also for the fundamental scientific aspect. The switching phenomena, observed in a CoFe PBA [3], were often ascribed due to a charge transfer between the $Co^{2+}(S = 3/2)$-$Fe^{3+}(S = 1/2)$ pairs and the $Co^{3+}(S = 0)$-$Fe^{2+}(S = 0)$ pairs through the cyanide C ≡ N bridge. In this interpretation, the low-spin (LS) Co^{3+} ($t_{2g}^6 e_g^0$, $S = 0$) ions are transformed to the high-spin (HS) Co^{2+} ($t_{2g}^5 e_g^2$, $S = 3/2$) ions [3,12–15]. In certain $Rb_xMn_z[Fe(CN)_6] \cdot m H_2O$ PBAs, a temperature (T)-induced phase transition with a large thermal hysteresis was observed [10,16,17]. Then, as in CoFe PBAs, the valence transition between the $Mn^{2+}(S = 5/2)−Fe^{3+}(S = 1/2)$ pairs at HT and the $Mn^{3+}(S = 2)$-$Fe^{2+}(S = 0)$ pairs at LT has been suggested for MnFe PBAs [6,10,16,17]. However, these models are controversial [3,9,12–17], and the experimental evidence for them is lacking. Therefore, in order to understand the origin of the switching phenomena in PBAs, it is crucial to determine the valence and spin states of M and M' ions experimentally.

X-ray absorption spectroscopy (XAS) is a powerful experimental tool for studying the valence and spin states of TM ions in solids [18,19]. Several studies on the valence states of M and M' ions in PBAs have been reported in the literature [7,8,12,17,20–22]. Some of the previous XAS studies on PBAs were done at the K edges of M and M' ions [7,8,12,17,22]. K-edge ($1s$) XAS for M and M' ions has the advantage of being bulk-sensitive because of the use of hard x rays. On the other hand, K-edge XAS does not reflect directly the valence

---

*Present address: KRISS, Daejeon 34113, Korea.
†Present address: Department of Physics, Mithibai College, Mumbai 400056, India.
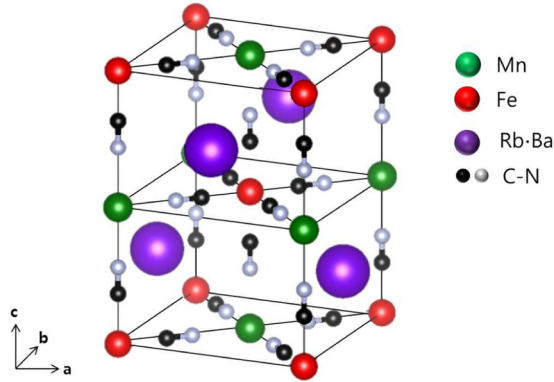‡kangjs@catholic.ac.kr

FIG. 1. Crystal structure of $(Rb_xBa_y)[MnFe(CN)_6] \cdot mH_2O$ compounds [11].

states of M and M' ions because it is determined mainly by the $1s \rightarrow 4p$ dipole-allowed transitions. In contrast, TM L-edge ($2p$) XAS provides more direct information on the valence and spin states of TM ions because the $2p \rightarrow 3d$ absorption process is involved. Soft x-ray magnetic circular dichroism (XMCD) is very unique in determining the spin and orbital components of the element-specific local magnetic moments of TM ions [23,24]. The K-edge XMCD [25–28] or the L-edge XMCD studies [29–31] have been reported for other kinds of PBAs. Further, there are several reports on the XAS/XMCD studies on PBA nanosystems [31–33].

In this work, we have studied the electronic structures of Ba-substituted $(Rb_xBa_y)Mn_z[Fe(CN)_6]$ PBAs ($z = [3 - (x + 2y)]/2$) (where mH_2O water molecules are omitted for clarity) by employing XAS and XMCD at the Mn and Fe L_3 ($2p_{3/2}$) and L_2 ($2p_{1/2}$) edges. $(Rb_xBa_y)Mn_z[Fe(CN)_6]$ PBAs exhibit a switching between the antiferromagnetic phase and the ferrimagnetic-like phase under an external magnetic field [34]. T-dependent variations of the Mn^{2+} and Fe^{3+} ordered magnetic moments were observed, but no structural transitions were observed in $(Rb_xBa_y)Mn_z[Fe(CN)_6]$ PBAs [11], so that the photoinduced magnetization transition is not expected.

II. EXPERIMENTAL DETAILS

Polycrystalline $(Rb_xBa_y)Mn_z[Fe(CN)_6]$ ($z = [3 - (x + 2y)]/2$) compounds with $(x,y) = (0.84,0),(0.69,0.19),$ $(0.19,0.3)$ were synthesized by a co-precipitation method. Figure 1 shows the tetragonal crystal structure of $(Rb_xBa_y)Mn_z[Fe(CN)_6]$ PBA at LT, which belongs to the $I\bar{4}m2$ space group. Lattice constants are $a = 7.45$ Å and $c = 10.55$ Å when $y = 0$ [11], and they decrease slightly with increasing Ba^{2+} concentration (y). Due to the stoichiometry of these compounds, some of the Fe, C, and N sites are vacant and the O atoms of H_2O molecules occupy the empty N sites. The main feature of this structure is the presence of the 3D network of Mn-NC-Fe chains along the (110) and (001) directions. Hence, depending on the relative orientations among the p_σ, p_π, Mn e_g and t_{2g}, and Fe t_{2g} orbitals, the ferromagnetic ordering in the ab plane and the antiferromagnetic ordering along the c axis are realized [11].

The details of the sample preparation and characterization are described in Ref. [11]. Hereafter, we will denote these

TABLE I. Labels of the $(Rb_xBa_y)Mn_z[Fe(CN)_6] \cdot mH_2O$ PBA samples, where the nominal values of $z = [3 - (x + 2y)]/2$ are listed. The average Fe valency v(Fe) is explained under Fig. 5.

$(Rb_xBa_y)Mn_z[Fe(CN)_6]$	x	y	z	v(Fe)
Rb0.84	0.84	0	1.08	2.75
Rb0.69	0.69	0.19	0.965	2.82
Rb0.19	0.19	0.3	1.105	2.75

samples as $(Rb_xBa_y)MnFe$ for simplicity, and we label them as Sample Rb0.84, Rb0.69, and Rb0.19 for $(x,y) = (0.84,0)$, $(0.69, 0.19)$, and $(0.19, 0.3)$, respectively (see Table I). For these samples, the Mn content is roughly ~ 1 for all three samples with small vacancies or excess. If one assumes Mn^{2+} and $[Fe(CN)_6]^{-3}$, the nominal z values of $z = 1.08, 0.965,$ and 1.105 are obtained, respectively.

XAS and XMCD experiments were performed at the 2A elliptically polarized undulator beamline of the Pohang Light Source (PLS). The chamber pressure was better than 3×10^{-10} Torr. Samples were mounted by using a carbon tape, and they were measured as they were. XAS and XMCD spectra were obtained by the total electron yield (TEY) via sample drain current, which has a probing depth of 50–100 Å [35]. XMCD spectra were obtained under an external magnetic field of $H \sim 0.6T$. The total resolution for XAS and XMCD was set at ~ 100 meV at $h\nu \sim 600$ eV. All the XAS and XMCD spectra were normalized to the incident photon flux.

III. RESULTS AND DISCUSSION

Figure 2(a) shows the measured Fe $2p$ (L-edge) XAS spectra of $(Rb_xBa_y)MnFe$ PBA samples. The Fe $2p$ XAS spectra of $(Rb_xBa_y)MnFe$ PBAs are very similar to one another, indicating that the valence states of Fe ions are very

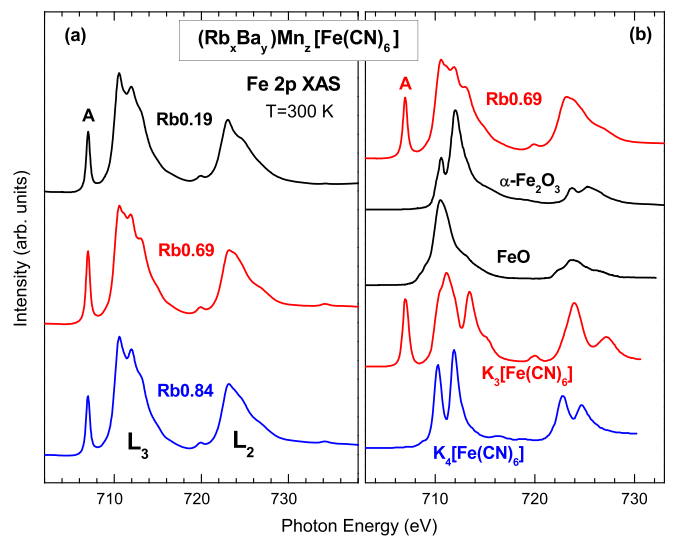FIG. 2. (a) Fe $2p$ XAS spectra of $(Rb_xBa_y)MnFe$ PBA samples. (b) Comparison of the Fe $2p$ XAS spectrum of Rb0.69 sample $[(x,y,z) = (0.69,0.19,0.965)]$ with those of Fe reference materials, such as trivalent α-Fe_2O_3, divalent FeO, trivalent $K_3[Fe^{3+}(CN)_6]$, and divalent $K_4[Fe^{2+}(CN)_6]$.
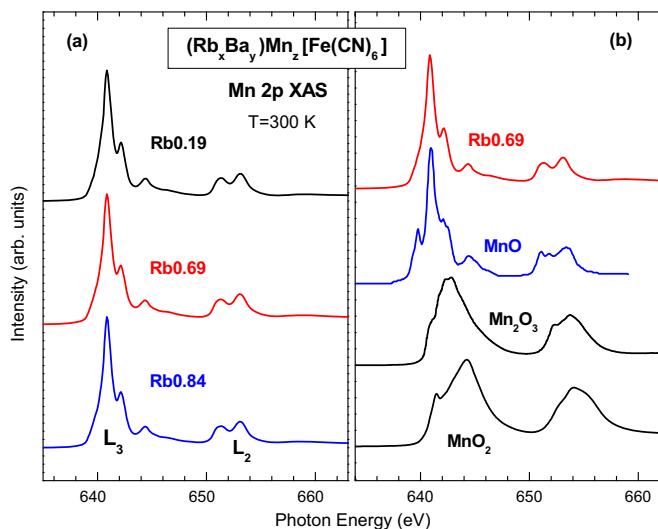
FIG. 3. (a) Mn $2p$ XAS spectra of $(Rb_xBa_y)MnFe$ PBAs. (b) Comparison of Mn $2p$ XAS spectra of the Rb0.69 sample with those of reference Mn oxides of MnS, MnO, Mn_2O_3, and MnO_2.

similar for different Ba substitutions. As a guide of the valence states of Fe ions, in Fig. 2(b) they are compared to those of divalent (Fe^{2+}) and trivalent (Fe^{3+}) reference materials, such as α-$Fe_2^{3+}O_3$ (Ref. [35]), $Fe^{2+}O$ (Ref. [36]), $K_3[Fe^{3+}(CN)_6]$ (Ref. [14]), and $K_4[Fe^{2+}(CN)_6]$ (Ref. [14]).

The Fe $2p$ XAS spectra of $(Rb_xBa_y)MnFe$ PBAs exhibit the features characteristic of a trivalent (Fe^{3+}) cyanide (CN) molecule of $K_3[Fe^{3+}(CN)_6]$, indicating that Fe ions are mainly trivalent in $(Rb_xBa_y)MnFe$ PBAs. In particular, the lowest-energy peak at $\sim$707 eV (peak A) [37] represents the trivalent Fe^{3+} state in $(Rb_xBa_y)MnFe$ PBAs. On the other hand, the Fe $2p$ XAS spectra of $(Rb_xBa_y)MnFe$ PBAs are quite different from those of Fe oxides of α-Fe_2O_3 and FeO. This finding implies that Fe ions in $(Rb_xBa_y)MnFe$ PBAs have a strong covalent bonding with $(C \equiv N)^{-1}$ ligands, but a very weak bonding with $O(H_2O)$. That is, the character of bonding of Fe ions with near neighbors in these $(Rb_xBa_y)MnFe$ PBAs is determined mainly by that with $(CN)^-$ ligands similarly as in $K_n[Fe(CN)_6]$ cyanide molecules.

A close look at Fig. 2(b) reveals that the line shapes of the Fe $2p$ XAS spectra of $(Rb_xBa_y)MnFe$ PBAs are slightly different from that of $K_3[Fe^{3+}(CN)_6]$ and that they indeed have some characteristic features of $K_4[Fe^{2+}(CN)_6]$. Such differences indicate that the valence states of Fe ions in $(Rb_xBa_y)MnFe$ PBAs are slightly Fe^{2+}-Fe^{3+} mixed-valent. This conclusion is supported by the cluster model analysis (see Fig. 5).

Figure 3(a) shows the measured Mn $2p$ XAS spectra of $(Rb_xBa_y)MnFe$ PBA samples. As a guide for the valence states of Mn ions, they are compared to those of divalent (Mn^{2+}), trivalent (Mn^{3+}), and tetravalent (Mn^{4+}) reference oxides in Fig. 3(b), such as $Mn^{2+}O$ (Ref. [38]), $Mn_2^{3+}O_3$ (Ref. [39]), and MnO_2 (Refs. [38,39]). Similarly as in Fe $2p$ XAS, the Mn $2p$ XAS spectra of $(Rb_xBa_y)MnFe$ PBAs are almost the same, suggesting that the valence states of Mn ions do not change for different Ba substitutions. Further, the Mn $2p$ XAS spectra of

$(Rb_xBa_y)MnFe$ PBAs are very similar to that of divalent MnO, suggesting that Mn ions are nearly divalent in $(Rb_xBa_y)MnFe$ PBAs. Differently from the Fe case, the Mn $2p$ XAS spectra of $(Rb_xBa_y)MnFe$ PBAs are very similar to that of solid MnO oxide, which has no $(CN)^-$ ligands, suggesting that Mn ions in $(Rb_xBa_y)MnFe$ have a weaker bonding to $(CN)^-$ ligands, in contrast to Fe ions. This conclusion is supported by the cluster model analysis (see Fig. 6). According to the crystal structure (see Fig. 1), Mn ions bond to the N side of the CN ligand, while Fe ions bond to the C side of the CN ligand, which may be the reason for the different bonding character of Fe and Mn ions in $(Rb_xBa_y)MnFe$ PBAs.

To understand the electronic structures of $(Rb_xBa_y)MnFe$ PBAs microscopically, we have analyzed the Fe and Mn $2p$ XAS spectra by employing the configuration-interaction (CI) cluster model calculations, where both the ligand-to-metal charge transfer (LMCT), i.e., the ligand-donor bonding, and the metal-to-ligand charge transfer (MLCT), i.e., the ligand-acceptor bonding, were included. LMCT and MLCT occur due to the π/σ donation and the π back-donation, respectively. A very pedagogical analysis for the Fe $2p$ XAS spectra of $K_3[Fe^{3+}(CN)_6]$ and $K_4[Fe^{2+}(CN)_6]$ cyanide molecules [20] and a similar analysis for Li-inserted $Li_xMn[Fe(CN)_6]$ PBA [21] have been reported. In the combined LMCT-MLCT charge-transfer multiplet (CTM) calculations, the free atomic multiplets due to the six CN ligand-ion environment are calculated by including the crystal-field energy $10Dq$, hybridization hopping parameters of V_{eg} and V_{t2g}, the repulsive $3d$-$3d$ Coulomb interaction U_{dd}, and the attractive $2p$-$3d$ Coulomb interaction U_{pd}. The energy levels of $3d$ orbitals are split by $10Dq$, corresponding to the energy separation between t_{2g} and e_g orbitals. The hybridization hopping parameters of V_{eg} and V_{t2g} take account of the covalency between TM $3d$ and ligand p states [18]. Namely, V_{eg} (V_{t2g}) corresponds to the hopping energy between Fe e_g (t_{2g}) and CN σ/π orbitals.

In these CI calculations, $U_{dd} = 2.0$ eV and $U_{pd} = 1.0$ eV were used for both Fe^{3+} and Fe^{2+} states. The charge-transfer (CT) parameters, employed in these calculations, are $EG2$, $EG3$, $EF2$, and $EF3$, where $EG2 \equiv E(d^{n-1}L^-) - E(d^n)$ and $EG3 \equiv E(d^{n-1}L^-) - E(d^{n+1}\underline{L})$ for ground-state MLCT and LMCT, respectively, and $EF2 \equiv E(\underline{c}d^{n-1}L^-) - E(\underline{c}d^n)$

TABLE II. Electronic structure parameters used in the LMCT-MLCT combined CTM calculations. The relationship between the final-state and ground-state energies is given by $EF = EG + U_{dd} - U_{pd}$ (U_{dd}: $3d$ on-site Coulomb energy, U_{pd}: core-hole potential) [20]. $EG2 \equiv d^{n-1}L^- - d^n$; $EG3 \equiv d^{n-1}L^- - d^{n+1}\underline{L}$; $EF2 \equiv \underline{c}d^{n-1}L^- - \underline{c}d^n$; $EF3 \equiv \underline{c}d^{n-1}L^- - \underline{c}d^{n+1}\underline{L}$, where $\underline{c}$, L^-, and $\underline{L}$ denote a core hole, an extra CN ligand electron, and a CN ligand hole, respectively. V_{eg} (V_{t2g}): the hopping energy for the e_g (t_{2g}) symmetry.

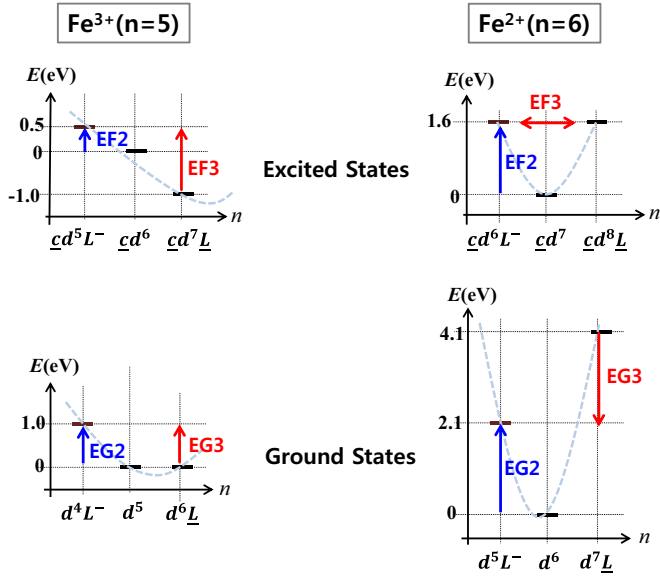| | | MLCT | | | | LMCT | | | |
	$10Dq$ (eV)	EG2 (eV)	EF2 (eV)	V_{eg} (eV)	V_{t2g} (eV)	EG3 (eV)	EF3 (eV)	V_{eg} (eV)	V_{t2g} (eV)
Fe^{3+} ($n = 5$)	3.0	1.0	1.0	0.5	0.9	2.0	1.0	1.5	2.1	0.6
Fe^{2+} ($n = 6$)	3.7	2.1	1.6	1.4	1.65	-2.0	0.0	1.4	0.6

FIG. 4. (a) The relative energy levels of the ground and final states for Fe^{3+} and Fe^{2+} valence states, obtained from the combined LMCT-MLCT calculations, as shown in Table II.

and $EF3 \equiv E(\underline{c}d^{n-1}L^-) - E(\underline{c}d^{n+1}\underline{L})$ for final-state MLCT and LMCT, respectively. Here $\underline{c}$, L^-, and $\underline{L}$ denote a Fe $2p$ core hole, an extra CN ligand electron, and a CN ligand hole, respectively.

Table II shows the parameter values used in the LMCT-MLCT CTM calculations, and Fig. 4 shows the relative energy

levels, corresponding to those parameters in Table II. The calculated Fe $2p$ XAS spectra for Fe^{2+}, Fe^{3+}, and the weighted sum of Fe^{2+} and Fe^{3+} are shown in Figs. 5(a)–5(c), and a comparison between the weighted sum and the measured Fe $2p$ XAS for the Rb0.69 sample is shown in Fig. 5(d). Here, the calculated multiplets are broadened with both the Gaussian and Lorentzian functions. The Lorentzian broadening, 2γ, describes the core-hole lifetime [40], while the Gaussian broadening (GB) simulates the instrumental resolution. In the calculated spectra, the value of GB = 0.1 eV was fixed (see Sec. II). Figure 5(d) shows that the weighted sum of Fe^{2+} and Fe^{3+}, with the area under Fe^{2+} and Fe^{3+} being 0.18 : 0.82, yields a good fitting to the measured Fe $2p$ XAS spectrum of the Rb0.69 PBA, corresponding to the average Fe valency of $v(Fe) = 2.82$. The $v(Fe)$ values for all $(Rb_xBa_y)MnFe$ PBA samples, obtained from the CI analysis, are listed in Table I.

The major findings of the CI cluster model calculations for Fe $2p$ XAS are as follows. First, the sharp, low-energy peak (A) corresponds to the trivalent Fe^{3+} states and arises from the large crystal-field energy ($10Dq \sim 3$ eV). Secondly, it is necessary to take into account both the LMCT and the MLCT in order to describe the measured Fe $2p$ XAS spectra of $(Rb_xBa_y)MnFe$ PBAs. Thirdly, Fe ions are found to be in the Fe^{2+}-Fe^{3+} mixed-valent states rather than in the purely integer-valence states, with the average valence states of $v(Fe) \sim 2.8$ in $(Rb_xBa_y)MnFe$ PBAs. This finding supports the previous finding of Fig. 2.

According to the energy level diagram (see Fig. 4), d^5 and $d^6\underline{L}$ configurations contribute almost equally to the Fe^{3+}
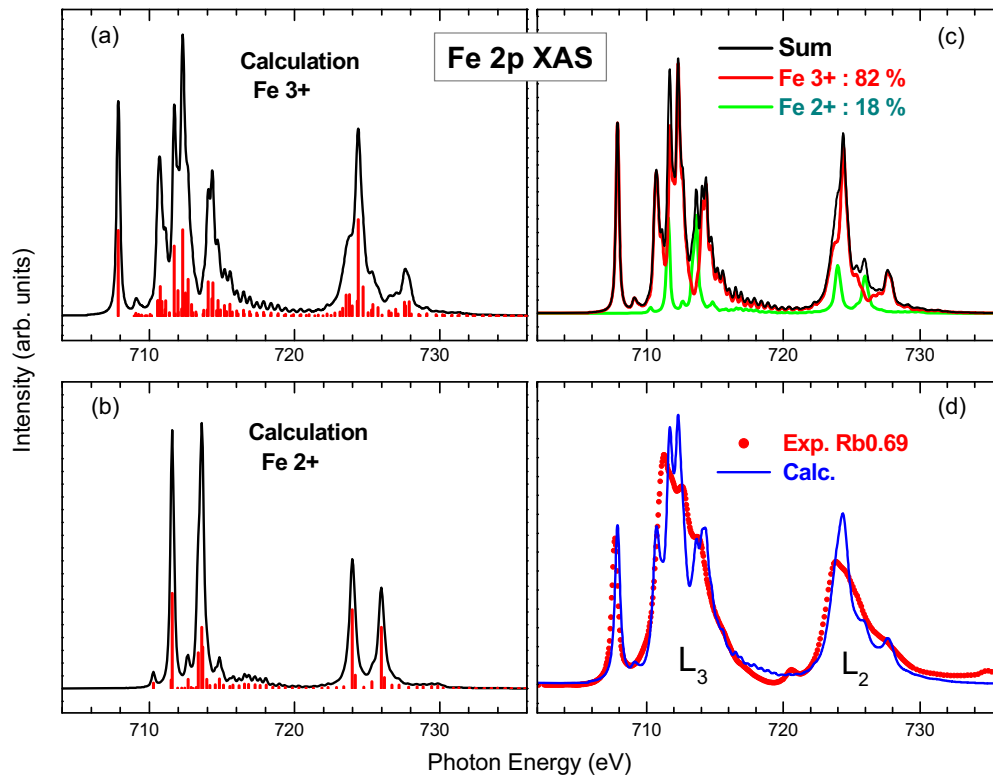

FIG. 5. The calculated $2p$ XAS spectra for (a) Fe^{3+}, (b) Fe^{2+}, and (c) the weighted sum of Fe^{2+} and Fe^{3+}, with the area ratio of $Fe^{2+} : Fe^{3+} = 0.18 : 0.82$, with GB = 0.1 eV and $2\gamma = 0.1/0.2$ eV for L_3/L_2. (d) The comparison between the weighted sum of the calculations and the measured Fe $2p$ XAS spectrum for the Rb0.69 PBA, where GB = 0.1 eV and $2\gamma = 0.2/0.4$ eV for L_3/L_2 are employed for the calculated XAS.
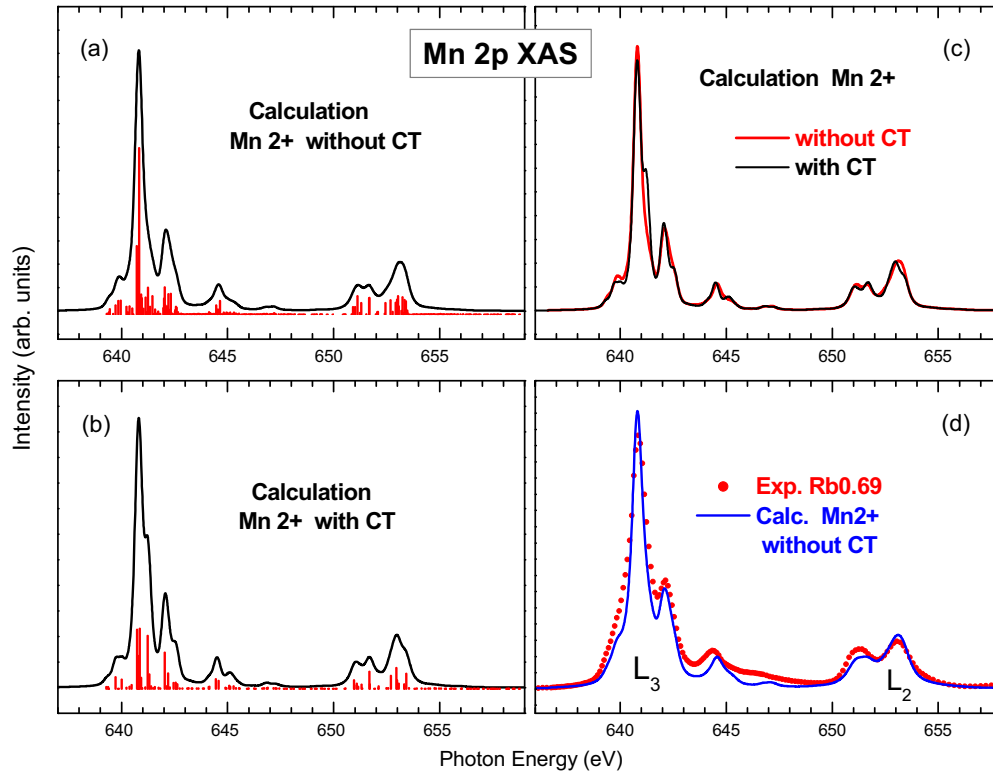
FIG. 6. The calculated Mn^{2+} $2p$ XAS spectra, obtained (a) without including CT, (b) including CT, and (c) a comparison between (a) and (b), with GB $= 0.1$ eV and $2\gamma = 0.1/0.2$ eV for L_3/L_2. (d) A comparison of the calculated Mn^{2+} XAS without CT with the measured Mn $2p$ XAS for the Rb0.69 PBA, where GB $= 0.1$ eV and $2\gamma = 0.2/0.4$ eV for L_3/L_2 are employed for the calculated XAS.

ground states, and the $\underline{c}d^7\underline{L}$ configuration is the lowest in the Fe^{3+} excited (final) states. Hence Fig. 4 shows that the trivalent Fe^{3+} ions have a strongly covalent bonding with $(C \equiv N)^{-1}$ ligands and that the effects of LMCT and MLCT are important in the Fe^{3+} states. In contrast, the Fe^{2+} ground and excited (final) states consist of nearly pure d^6 and $\underline{c}d^7$ configurations, respectively, indicating that the effects of LMCT and MLCT are negligible for the Fe^{2+} states.

Figure 6 shows the calculated Mn $2p$ XAS spectra: (a) and (b) show the Mn $2p$ XAS for Mn^{2+}, calculated without and with including CT, respectively, (c) shows a comparison between (a) and (b), and (d) shows a comparison between the calculated Mn^{2+} XAS without CT and the measured Mn $2p$ XAS for the Rb0.69 PBA. For these calculations, $10Dq = 0.6$ eV was employed. For the calculation including CT, $U_{dd} = 5.2$ eV, $U_{pd} = 6.2$ eV, and $\Delta = 6.5$ eV were employed, where Δ is the energy needed to transfer one electron from the CN ligand band to the Mn $3d$ orbital. Similarly as in Fe $2p$ calculations (Fig. 5), GB $= 0.1$ eV was fixed for all the calculated spectra to simulate the instrumental resolution (see Sec. II). The same 2γ values as for the Fe $2p$ XAS calculations were used for the Mn $2p$ XAS calculations [40].

According to Fig. 6, the calculated Mn^{2+} spectrum with $10Dq = 0.6$ eV describes the measured Mn $2p$ XAS spectra of $(Rb_xBa_y)MnFe$ PBA very well. Further, the calculated Mn^{2+} spectrum, obtained by including CT, is very similar to that obtained without including CT, indicating that the effect of CT is negligible for the Mn^{2+} ions in $(Rb_xBa_y)MnFe$ PBA.

This makes a sharp contrast to the Fe^{3+} ions in $(Rb_xBa_y)MnFe$ PBA.

As shown in Fig. 7, finite Mn $2p$ XMCD signals are observed in $(Rb_xBa_y)MnFe$ PBAs even though they are very weak, whereas the measured Fe $2p$ XMCD signals are almost zero (not shown in this paper). In Fig. 7(a), Mn $2p$ XMCD spectra of three different $(Rb_xBa_y)MnFe$ PBAs are compared, which indicates that the XMCD line shapes are very similar to one another. In Fig. 7(b), the Mn $2p$ XAS and XMCD spectra of the Rb0.69 PBA are shown as a typical example. Then, Fig. 7(c) compares the Mn $2p$ XMCD spectrum of Rb0.69 with that of a divalent (Mn^{2+}) ferrimagnetic Mn oxide $MnFe_2O_4$ as a reference [41]. The intensities of the Mn $2p$ XMCD signals, with respect to the Mn $2p$ XAS signals, $I(\Delta\rho)/I(XAS)$, are plotted in Fig. 7(d), which shows that $I(\Delta\rho)/I(XAS)$ does not change much for different Ba concentrations.

Note that the very weak ($\sim 0.4\%$) but finite Mn $2p$ XMCD signals are observed in all of $(Rb_xBa_y)MnFe$ PBAs above the Néel temperature ($T_N \sim 10.6$–13.5 K) [11] [see Fig. 7(d)]. We think that this is because the magnetic moments of Mn ions are locally aligned due to the applied magnetic field during XMCD measurements. In addition, the XMCD line shapes are very similar to that of ferrimagnetic spinel oxide of divalent $MnFe_2O_4$, where Mn ions are in the HS states [41]. Hence the measured Mn $2p$ XMCD spectra for $(Rb_xBa_y)MnFe$ PBAs confirm the HS Mn^{2+} states ($t_{2g}^3 e_g^2$, $S = 5/2$). On the other hand, the negligibly weak Fe $2p$ XMCD signals in $(Rb_xBa_y)MnFe$ PBAs (not shown in this paper) suggest that Fe ions are in the LS states of Fe^{3+} ($t_{2g}^5 e_g^0$, $S = 1/2$) and

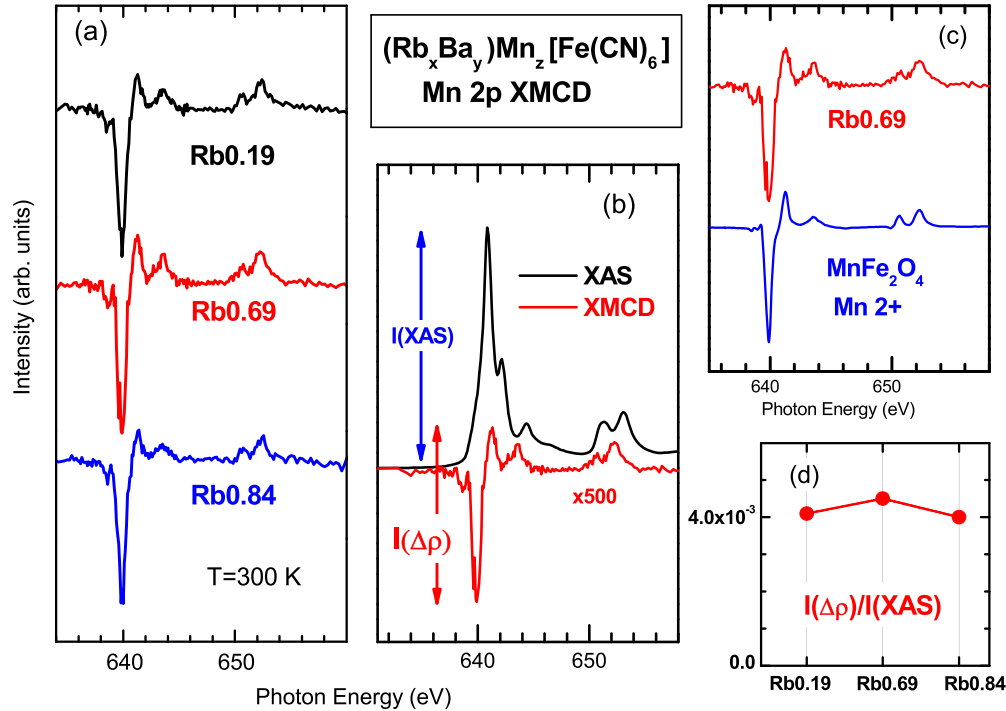FIG. 7. (a) Mn $2p$ XMCD spectra of $(Rb_xBa_y)MnFe$ PBAs. (b) Typical Mn $2p$ XAS and XMCD spectra of a Rb_xBa_yMnFe (Rb0.69) PBA. (c) Comparison of the Mn $2p$ XMCD spectrum of the Rb0.69 PBA with that of a divalent reference oxide of $MnFe_2O_4$ (Mn^{2+}). (d) Intensity plots of Mn $2p$ XMCD signals with respect to those of XAS, $I(\Delta\rho)/I(XAS)$, for $(Rb_xBa_y)MnFe$ PBAs. $I(\Delta\rho)$ and $I(XAS)$ are denoted in (b).

Fe^{2+} ($t_{2g}^6 e_g^0$, $S = 0$), respectively. To determine the spin and orbital magnetic moments of Mn ions, we have analyzed the Mn $2p$ XMCD spectra using the XMCD sum rule [23,24,42]. The results from the sum-rule analysis are summarized in Table III. They show that the orbital magnetic moments m_{orb} of Mn ions are negligibly small in $(Rb_xBa_y)MnFe$ PBAs ($m_{orb}/m_{spin} < 3\%$).

We now discuss the T-dependent electronic structures of $(Rb_xBa_y)MnFe$ PBAs. Figure 8 shows the T-dependent Fe $2p$ and Mn $2p$ XAS spectra of $(Rb_xBa_y)MnFe$ PBA for Rb0.69 in the temperature range of $80 \leqslant T \leqslant 300$ K. Due to the charging problem in these PBA samples [43], the spectra obtained at low T are not good. For example, those at $T = 150$ K are very noisy, and the Fe $2p$ XAS line shape at 80 K is bad. Even though some data are noisy, Fig. 8 shows clearly that the line shapes of both the Fe $2p$ and Mn $2p$ XAS spectra are essentially the same between $80 \leqslant T \leqslant 300$ K, reflecting that the Fe^{2+}-Fe^{3+} mixed-valent states and Mn^{2+} states do

not change for $T \geqslant \sim 80$ K. Thus the T-dependent XAS study provides evidence that our $(Rb_xBa_y)MnFe$ PBA samples do not undergo charge transfer upon cooling. It is noteworthy that, according to Fe K edge XAS at $T = 300$ K, the Fe ions in switchable $RbMnFe(CN)_6$ are also Fe^{2+}-Fe^{3+} mixed-valent [17]. This feature suggests that a simple integer charge transfer upon cooling from Fe^{3+}-CN-Mn^{2+} to Fe^{2+}-CN-Mn^{3+} might not occur even in switchable MnFe PBAs, as proposed earlier [6,16,17]. A further XAS/XMCD study at very low temperature would be highly desirable to resolve the issue for the origin of the photoinduced transition in PBAs. As explained in Ref. [43], it is very challenging to overcome the severe charging problem in the XAS/XMCD study of PBA samples.

IV. CONCLUSIONS

The electronic structures of $(Rb_xBa_y)MnFe$ PBAs have been investigated by employing synchrotron-radiation-excited XAS and XMCD, and the measured XAS spectra have been analyzed with the CI cluster model calculations. We have found that Fe ions are Fe^{2+}-Fe^{3+} mixed-valent, with the Fe average valency of $v(Fe) \sim 2.8$, and in LS configurations, while Mn ions are nearly divalent and in HS states. According to the CI cluster model analysis, it is necessary to take into account both the LMCT and the MLCT in describing Fe $2p$ XAS, while the effect of CT is negligible in describing Mn $2p$ XAS. The trivalent Fe^{3+} ions are found to have a strong covalent bonding

TABLE III. The spin and orbital magnetic moments of the divalent Mn^{2+} ions in $(Rb_xBa_y)Mn_z[Fe(CN)_6]$ PBAs (given in units of μ_B/atom).

	m_{spin}	m_{orb}	m_{orb}/m_{spin}
Rb0.84	8.6×10^{-3}	1.86×10^{-4}	0.022
Rb0.69	6.5×10^{-3}	1.48×10^{-4}	0.023
Rb0.19	8.4×10^{-3}	1.64×10^{-4}	0.020
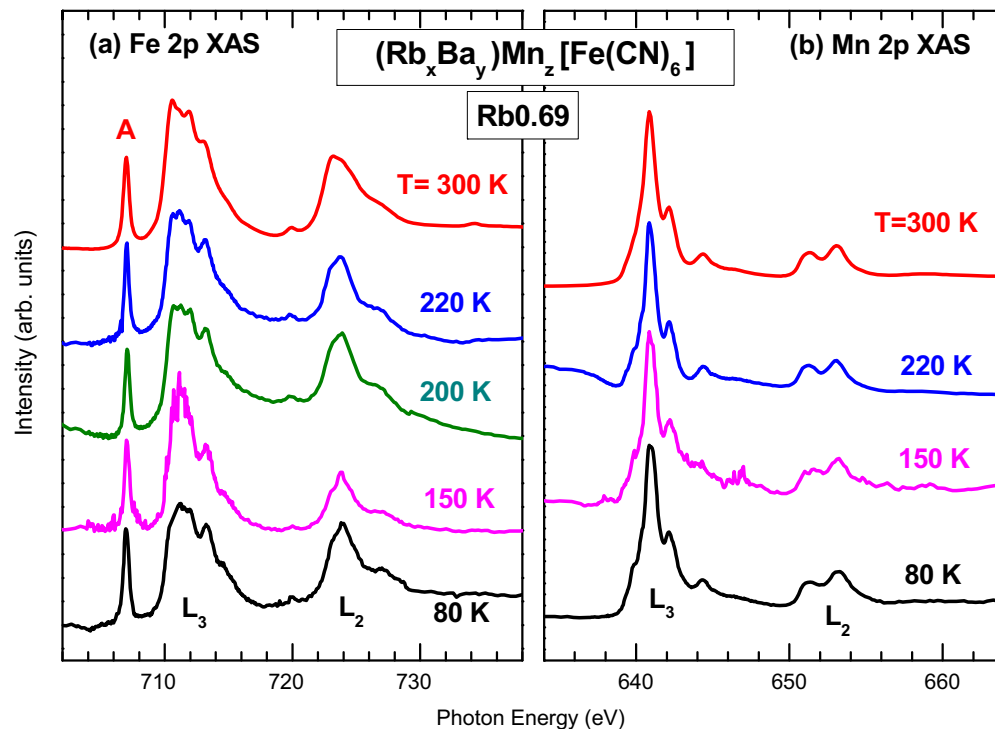
FIG. 8. Temperature (T)-dependent XAS spectra of $(Rb_xBa_y)MnFe$ PBA (Rb0.69) for $80 \leqslant T \leqslant 300$ K. (a) T-dependent Fe $2p$ XAS spectra. (b) T-dependent Mn $2p$ XAS spectra.

with the $C \equiv N$ ligands and to be under a large crystal-field energy of $10Dq \sim 3$ eV. In contrast, the divalent Mn^{2+} ions are found to have a weak covalency effect and to be under a small $10Dq \sim 0.6$ eV. The measured Mn and Fe $2p$ XMCD spectra for $(Rb_xBa_y)MnFe$ support the HS Mn^{2+} states ($t_{2g}^3 e_g^2$; $S = 5/2$) and the LS Fe^{2+} ($t_{2g}^6 e_g^0$; $S = 0$)-Fe^{3+} ($t_{2g}^5 e_g^0$, $S = 1/2$) states, respectively. The T-dependent Fe $2p$ and Mn $2p$ XAS spectra are essentially the same for $80 \leqslant T \leqslant 300$ K. These findings suggest that a simple integer-valence transition model

proposed for the photoinduced magnetization transitions in MnFe PBAs needs to be reexamined more carefully.

[1] J. M. Manriquz, G. T. Yee, R. S. Mclean, A. J. Epstein, and J. S. Miller, Science **252**, 1415 (1991).

[2] S. Ferlay, T. Mallah, R. Ouahes, P. Veillet, and M. Verdaguer, Nature (London) **378**, 701 (1995).

[3] O. Sato, T. Iyoda, A. Fujishima, and K. Hashimoto, Science **272**, 704 (1996).

[4] S.-i. Ohkoshi, T. Iyoda, A. Fujishima, and K. Hashimoto, Phys. Rev. B **56**, 11642 (1997).

[5] E. Coronado, M. C. Giménez-López, G. Levchenko, F. M. Romero, V. García-Baonza, A. Milner, and M. Paz-Pasternak, J. Am. Chem. Soc. **127**, 4580 (2005).

[6] S.-i. Ohkoshi, H. Tokoro, and K. Hashimoto, Coord. Chem. Rev. **249**, 1830 (2005).

[7] D. Aguilá, Y. Prado, E. S. Koumousi, C. Mathoniére, and R. Clérac, Chem. Soc. Rev. **45**, 203 (2016).

[8] A. Bleuzen, C. Lomenech, V. Escax, F. Villaim, F. Varret, C. Cartier dit Moulin, and M. Verdaguer, J. Am. Chem. Soc. **122**, 6648 (2000).

[9] M. K. Saha, M. C. Morón, F. Palacio, and I. Bemal, Inorg. Chem. **44**, 1354 (2005).

[10] H. Tokoro, T. Matsuda, T. Nuida, Y. Moritomo, K. Ohoyama, E. Davy, L. Dangui, K. Boukheddaden, and S.-i. Ohkoshi, Chem. Mater. **20**, 423 (2008).

[11] N. Thakur, S. M. Yusuf, P. L. Paulose, and L. Keller, J. Appl. Phys. **111**, 063908 (2012).

[12] V. Escax, A. Bleuzen, C. Cartier dit Moulin, F. Villain, A. Goujon, F. Varret, and M. Verdaguer, J. Am. Chem. Soc. **123**, 12536 (2001).

[13] N. Shimamoto, S. Ohkoshi, O. Sato, and K. Hashimoto, Inorg. Chem. **41**, 678 (2002).

[14] C. C. dit Moulin, F. Villain, A. Bleuzen, M.-A. Arrio, P. Sainctavit, C. Lomenech, V. Escax, F. Baudelet, E. Dartyge, J.-J. Gallet, and M. Verdaguer, J. Am. Chem. Soc. **122**, 6653 (2000).

[15] S. Bonhommeau, N. Pontius, S. Cobo, L. Salmon, F. M. F. de Groot, G. Molnar, A. Bousseksou, H. A. Kurr, and W. Eberhardt, Phys. Chem. Chem. Phys. **10**, 5882 (2008).

[16] H. Tokoro, S. Miyashita, K. Hashimoto, and S.-i. Ohkoshi, Phys. Rev. B **73**, 172415 (2006).

[17] T. Yokoyama, H. Tokoro, S.-i. Ohkoshi, K. Hashimoto, K. Okamoto, and T. Ohta, Phys. Rev. B **66**, 184111 (2002).

[18] F. M. F. de Groot, J. C. Fuggle, B. T. Thole, and G. A. Sawatzky, Phys. Rev. B **42**, 5459 (1990).

[19] G. van der Laan and I. W. Kirkman, J. Phys.: Condens. Matter **4**, 4189 (1992).

[20] R. K. Hocking, E. C. Wasinger, F. M. F. de Groot, K. O. Hodgson, B. Hedman, and E. I. Solomon, J. Am. Chem. Soc. **128**, 10442 (2006).

[21] D. Asakura, M. Okubo, Y. Mizuno, T. Kudo, H. Zhou, K. Amemiya, F. M. F. de Groot, J.-L. Chen, W.-C. Wang, P.-A. Glans, C. Chang, J. Guo, and I. Honma, Phys. Rev. B **84**, 045117 (2011).

[22] S. Adak, M. Hartl, L. Daemen, E. Fohtung, and H. Nakotte, J. Electron Spectrosc. Relat. Phenom. **214**, 8 (2017).

[23] B. T. Thole, P. Carra, F. Sette, and G. van der Laan, Phys. Rev. Lett. **68**, 1943 (1992).

[24] C. T. Chen, Y. U. Idzerda, H.-J. Lin, N. V. Smith, G. Meigs, E. Chaban, G. H. Ho, E. Pellegrin, and F. Sette, Phys. Rev. Lett. **75**, 152 (1995).

[25] M. Verdaguer, T. Mallah, C. Hélary, F. L'Hermite, P. Sainctavit, M. A. Arrio, D. Babel, F. Baudelet, E. Dartyge, and A. Fontaie, Physica B **208**, 765 (1995).

[26] E. Dujardin, S. Ferlay, X. Phan, C. Desplanches, C. Cartier dit Moulin, P. Sainctavit, F. Baudelet, E. Dartyge, P. Veillet, and M. Verdaguer, J. Am. Chem. Soc. **120**, 11347 (1998).

[27] G. Champion, V. Escax, C. Cartier dit Moulin, A. Bleuzen, F. Villain, F. Baudelet, E. Dartyge, and M. Verdaguer, J. Am. Chem. Soc. **123**, 12544 (2001).

[28] J.-D. Cafun, J. Lejeune, J.- Paul Itié, F. Baudelet, and A. Bleuzen, J. Phys. Chem. C **117**, 19645 (2013).

[29] E. Coronado, M. Carmen Giménez-López, T. Korzeniak, G. Levchenko, F. M. Romero, A. Segura, V. García-Baonza, J. C. Cezar, F. M. F. de Groot, A. Milner, and M. Paz-Pasternak, J. Am. Chem. Soc. **130**, 15519 (2008).

[30] M.-A. Arrio, J. Long, C. Cartier dit Moulin, A. Bachschmidt, V. Marvaud, A. Rogalev, C. Mathoniére, F. Wilhelm, and P. Sainctavit, J. Phys. Chem. C **114**, 593 (2010).

[31] Y. Prado, M.-A. Arrio, F. Volatron, E. Otero, C. Cartier dit Moulin, P. Sainctavit, L. Catala, and T. Mallah, Chem. Eur. J. **19**, 6685 (2013).

[32] M. L. Baker, Y. Kitagawa, T. Nakamura, K. Tazoe, Y. Narumi, Y. Kotani, F. Iijima, G. N. Newton, M. Okumura, H. Oshio, and H. Nojiri, Inorg. Chem. **52**, 13956 (2013).

[33] S. Kang, H. Zheng, T. Liu, K. Hamachi, S. Kanegawa, K. Sugimoto, Y. Shiota, S. Hayami, M. Mito, T. Nakamura, M. Nakano, M. L. Baker, H. Nojiri, K. Yoshizawa, C. Duan, and O. Sato, Nat. Commun. **6**, 5955 (2015).

[34] S. M. Yusuf, N. Thakur, M. Medarde, and L. Keller, J. Appl. Phys. **112**, 093903 (2012).

[35] J.-Y. Kim, T. Y. Koo, and J.-H. Park, Phys. Rev. Lett. **96**, 047205 (2006).

[36] T. J. Regan, H. Ohldag, C. Stamm, F. Nolting, J. Lüning, J. Stöhr, and R. L. White, Phys. Rev. B **64**, 214422 (2001).

[37] After the exposure to the soft x-ray synchrotron radiation, the radiation damage was observed in these $(Rb_x Ba_y)$MnFe PBA samples. But we have checked that the existence of the Fe^{2+} valence states is intrinsic to the bulk of $(Rb_x Ba_y)$MnFe PBAs and that the Mn^{2+} valence states are very stable in $(Rb_x Ba_y)$MnFe PBAs under external perturbations.

[38] C. Mitra, Z. Hu, P. Raychaudhuri, S. Wirth, S. I. Csiszar, H. H. Hsieh, H.-J. Lin, C. T. Chen, and L. H. Tjeng, Phys. Rev. B **67**, 092404 (2003).

[39] P. Ghigna, A. Campana, A. Lascialfari, A. Caneschi, D. Gatteschi, A. Tagliaferri, and F. Borgatti, Phys. Rev. B **64**, 132413 (2001).

[40] To show the multiplet structures better, rather small values of $2\gamma = 0.1$eV/0.2eV were used for L_3/L_2 in Figs. 5(a)–5(c). Then, in comparison to the measured spectrum, the 2γ value was adjusted to fit the measured peak widths, resulting in $2\gamma = 0.2$eV/0.4eV for L_3/L_2 [see Figs. 5(d) and 6(d)].

[41] J.-S. Kang, G. Kim, H. J. Lee, D. H. Kim, H. S. Kim, J. H. Shim, S. Lee, H. G. Lee, J.-Y. Kim, B. H. Kim, and B. I. Min, Phys. Rev. B **77**, 035121 (2008).

[42] D. H. Kim, E. Lee, H. W. Kim, S. Seong, S.-M. Yang, H.-S. Park, J. P. Hong, Y. Kim, J.-Y. Kim, and J.-S. Kang, J. Magn. Magn. Mater. **432**, 450 (2017).

[43] These PBS samples exhibit severe charging problems, and it was difficult to obtain the reliable XAS and XMCD spectra at low temperature ($T \leqslant \sim 250$ K). We have not succeeded in obtaining the reliable XMCD spectra at $T \leqslant \sim 250$ K. To overcome a severe charging problem in the XAS/XMCD study of these PBA samples would be very challenging.